Operando Investigations of the Solid Electrolyte Interphase in the Lithium Mediated Nitrogen Reduction Reaction

Niklas H. Deissler[a], J. Bjarke V. Mygind[a], Katja Li[a], Valerie A. Niemann[b], Peter Benedek[b], Valentin Vinci[c], Shaofeng Li[a], Xianbiao Fu[a], Peter C. K. Vesborg[a], Thomas F. Jaramillo[b], Jakob Kibsgaard[a], Jakub Drnec[c], Ib Chorkendorff*[a]

Abstract

The lithium-mediated nitrogen reduction reaction (Li-NRR) represents a promising approach for electrochemical nitrogen activation, in which the solid electrolyte interphase (SEI) layer formed on the electrochemically plated lithium plays a key role. Herein, we used time-resolved, operando, grazing incidence wide-angle X-ray scattering (GI WAXS) to identify SEI species and reaction intermediates in the Li-NRR, comparing $LiBF_4$ and $LiClO_4$ as electrolyte salts. We demonstrated how the SEI composition influences the Li-NRR performance by regulating proton transport to the plated Li. When $LiBF_4$ is used as electrolyte salt, the formation of LiF and Lithium ethoxide (LiEtO) is observed. Reaction intermediates such as LiH and LiN_xH_y species were found and provide insight into reaction pathways towards undesired and desired products, respectively. Observed restructuring of the Cu (111) single crystal substrate also indicates interaction with plated Li that could possibly influence the Li-NRR performance. Together, these experiments give molecular insight on how to design Li-NRR systems and their SEI layers for optimal performance.

[a] Department of Physics, Technical University of Denmark, Kongens Lyngby, Denmark.
[b] Department of Chemical Engineering, Stanford University, Stanford, CA, USA. SUNCAT Center for Interface Science and Catalysis, SLAC National Accelerator Laboratory, Menlo Park, CA, USA
[c] Experimental Division, European Synchrotron Radiation Facility, Grenoble, France.

† Electronic Supporting Information (ESI) available: Detailed Experimental methods, Photos of setup, Electrochemical data, 1D Diffractograms of all experiments, Time traces of all species, Time development of 2D detector images of all species, XPS data

Introduction

Every year, more than 180 million tons of ammonia are produced, mainly for use as fertilizer.[1] In the future, ammonia might prove suitable as an energy carrier to replace fossil fuels.[2] Currently, ammonia is produced almost exclusively in the Haber-Bosch process, which requires elevated temperatures and pressures (400 °C - 450 °C, 150 - 200 bar).[3] Electrochemical processes have been considered as alternatives for many years, however, progress was hindered by many erroneous reports.[4] The lithium-mediated nitrogen reduction reaction (Li-NRR) was first reported in 1930 by Fichter et al.[5] and later by Tsuneto et al.[6,7] in 1993. Despite these reports, there was no subsequent exploration or follow-up on this discovery. In 2019 our group established the Li-NRR as the only reliable strategy for electrochemical ammonia production from elemental nitrogen (N_2).[8] In the Li-NRR, lithium (Li) is plated on the cathode from an electrolyte consisting of an organic solvent, typically tetrahydrofuran (THF), a lithium-containing salt, and a proton carrier, usually ethanol (EtOH). Plated Li can react with N_2 to form intermediate Li-N- compounds, which can be protonated by the proton carrier thereby forming ammonia.[9,10] Plated Li also reacts with the electrolyte to form the solid electrolyte interphase (SEI) layer;[11] however, its composition and function are mostly unknown. There have been substantial efforts aiming at a better understanding of the role of the SEI, though most studies rely on ex-situ techniques.[12–16] In situ investigations of the SEI by means of neutron reflectometry and grazing incidence wide-angle X-ray scattering (GI WAXS) have been conducted only with $LiClO_4$ as electrolyte salt at current densities below 1 mA cm^{-2}.[17,18]

Recent research driven by the growing interest in Li-NRR has led to significantly increased Faradaic efficiencies (FE) and current densities.[12,19,20] Further, the development of flow-cell systems and the implementation of hydrogen on the anode enables continuous ammonia synthesis without the reliance on sacrificial agents.[13,21] In early studies mainly lithium perchlorate ($LiClO_4$) was used as electrolyte salt.[6–9,11,12] Recent studies by our group using a pressurized one-compartment cell as well as a flow cell

employed lithium tetrafluoroborate ($LiBF_4$) as an alternative electrolyte salt, attributing improved performances to the SEI structure and composition.[13,20] To date, however, the SEI layer in the $LiBF_4$-based electrolyte has only been characterized ex-situ[14,20], and it remains to be determined how it enables enhanced NH_3 selectivity and stability compared to the $LiClO_4$-based electrolyte.

In this work, we present an operando GI WAXS study of the SEI in the Li-NRR with $LiBF_4$ as electrolyte salt. GI WAXS was used to characterize the crystalline deposits on a Cu (111) single crystal working electrode during the LI-NRR using $LiClO_4$ or $LiBF_4$ with or without proton donor, EtOH, thereby enabling us to monitor Li^0 and its reaction with the electrolyte, EtOH, and N_2. These in-situ X-ray measurements have the benefit of detecting transient species that are not possible to observe ex-situ. We found that a LiF containing SEI layer formed by $LiBF_4$, stabilizes the plated Li by limiting proton transport to the electrode. Intermediate LiN_xH_y species as well as LiH were detected, giving insight into reaction pathways towards both desired and undesired products. The formation of Li_2CO_3, likely related to electrolyte degradation was observed with $LiClO_4$. This work provides molecular understanding of the SEI layer to guide further development of Li-NRR towards higher selectivities and stabilities, including the rational design of artificial SEIs, which to date, have not been explored in this system.

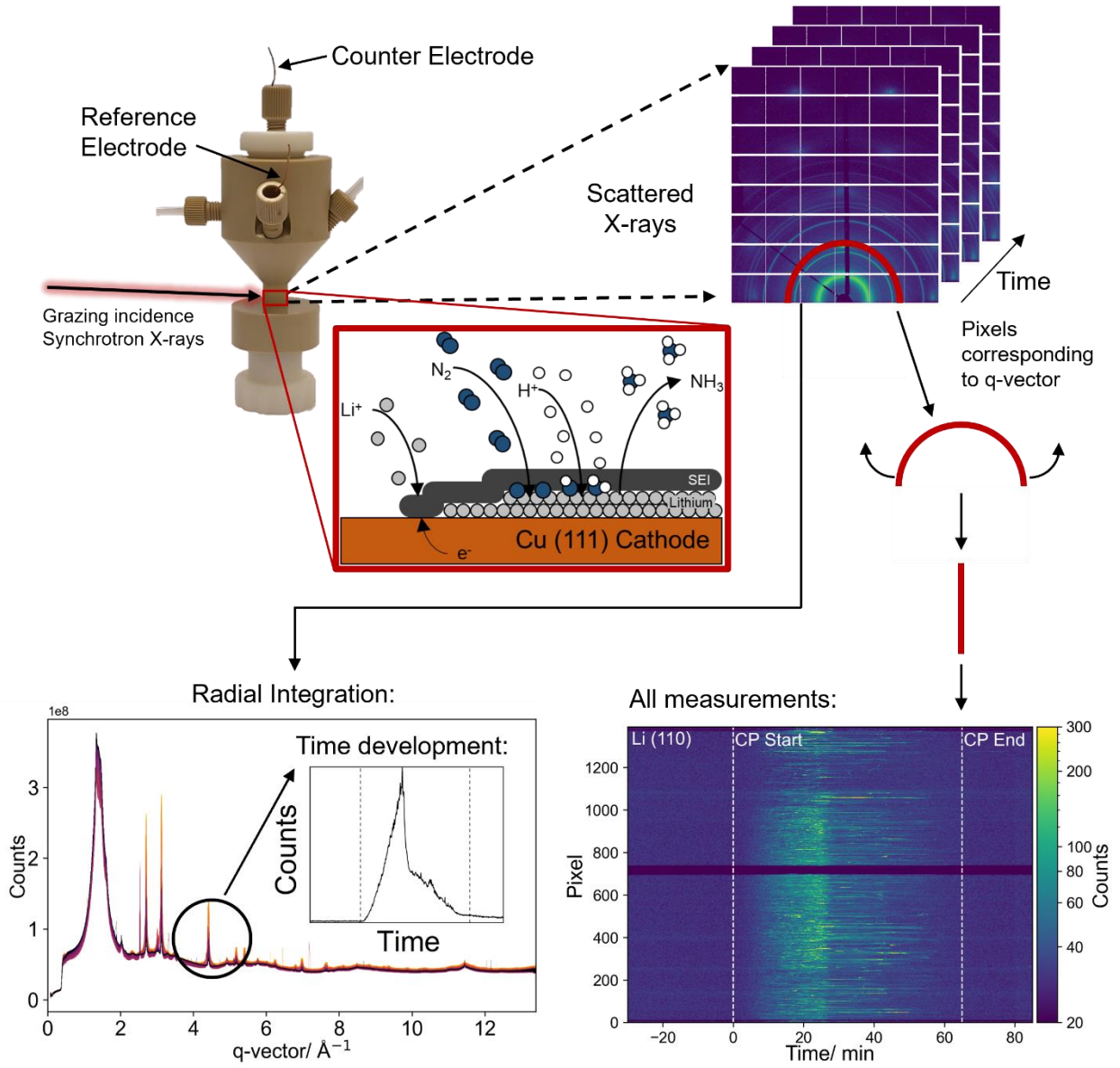

Figure 1: Schematic of the experimental setup and the data processing. Synchrotron X-rays are directed in grazing incidence on a Cu (111) single crystal working electrode used for the lithium-mediated nitrogen reduction reaction. 2D detector images, obtained from the diffracted X-rays, were integrated, giving diffraction patterns, and used to identify SEI components. Pixels corresponding to a specific q-vector were plotted with time, where t=0 is set to the beginning of a chronopotentiometry (CP) measurement.

Experimental

With each electrolyte composition, $LiBF_4$ (1 M) or $LiClO_4$ (1 M) in THF, both with EtOH or without EtOH (1 vol% vs. 0 vol%), two synchrotron experiments were conducted. A Cu (111) single crystal was used as working electrode, a Pt-mesh as counter electrode and a $LiFePO_4$ (LFP) electrode as reference.[22,23] All

operando measurements were conducted at the ID31 beamline at the European Synchrotron Radiation Facility (ESRF). The experimental setup and subsequent data treatment are shown schematically in Figure 1. The Cu (111) single crystal electrode was aligned to minimize its contribution to the recorded detector images. Following an initial period (>25 min) of open circuit voltage (OCV) a linear sweep voltammetry (LSV) with a scan rate of 20 mV s^{-1} was conducted until Li-plating potential was reached. Subsequently Chronopotentiometry (CP) at -2 mA cm^{-2} was carried out for 65 min, followed by another OCV measurement (>20 min). Recording of GI WAXS measurements began when the initial OCV measurement was started. Detector images recorded every 5-10 s were radially integrated giving 1D diffractograms as shown in Figure 1. Following the intensity of a given peak over time gives information about the time development of the corresponding species. Additionally, the time development of the detector image pixels provides insights into the crystallinity of corresponding species. Experimental details can be found in the electronic supplementary information (ESI) (Fig. S1, ESI).

Results & Discussion

Figure 2A shows the peaks corresponding to the Li (110) reflection, exemplarily for all Li reflections, while the time development of the maximum intensity of the peaks is shown in Figure 2B. Diffractograms showing different q-ranges and reference patterns are shown in the ESI (Fig. S2-S26, ESI) In experiments without EtOH, the intensity of the Li (110) peak increased continuously while current was applied. When measuring at OCV after the CP, the peak intensity decreased only slowly, indicating that the plated Li remained on the electrode surface, dissolving only slowly. Accordingly, the working electrode potentials shown in Figure 2C did not increase within the first 20 min after the CP when no EtOH was present in the electrolyte. Corresponding counter electrode potentials are shown in the ESI (Fig. S27, ESI) as well as LSV measurements and electrochemical data for all experiments (Fig. S28- S43, ESI). The observed FEs for ammonia without EtOH, 0.1 ± 0.1 % and 0.4 ± 0.4 % for $LiClO_4$ and $LiBF_4$

respectively, are in agreement with previously reported values for unpressurized batch reactors.[6,7,10,24,25] The stability of the plated Li indicates that also the competing reduction of protons by Li ($\mathrm{Li} + \mathrm{H}^+ \rightarrow \mathrm{Li}^+ + \frac{1}{2}\mathrm{H}_2$) is limited.

When an electrolyte with 1M $LiClO_4$ and 1 vol% EtOH was used, the Li (110) peak only appeared temporarily and was absent throughout most of the measurement. This only *transient* appearance suggests that Li is plated but then converted by fast reactions. Correspondingly, the working electrode potential increased almost immediately after the end of the CP (Fig. 2C). The low FE of 2±1 %, observed for this system, suggests that the main reaction is the hydrogen-forming reduction of protons by Li ($Li + H^+ \rightarrow Li^+ + \frac{1}{2}H_2$). Since only a small volume (1.1 mL) of N_2 saturated electrolyte without flow or stirring could be used in the in-operando cell, a shortage of N_2 at the electrode can likely explain the low FE.[9–11]

When $LiBF_4$ was used as electrolyte salt (FE=3±2 %), lithium remained on the electrode for a prolonged time even in the presence of EtOH (Fig. 2B). Nevertheless, after an initial continuous increase for 25 mins, the peak intensity decreased until the end of the CP, indicating that Li was consumed in reactions. After the CP, the working electrode potential remained at -3.4 V vs. LFP for 10 min, indicating that some Li was still present on the electrode[22] even though it could not be detected by WAXS. Furthermore, in all electrolytes, when Li is detected, the intensity increase is not uniform over all corresponding pixels on the detector (S44-S51, ESI) and thus it is likely that Li does not form a fully polycrystalline phase but rather forms fewer larger crystallites. Therefore, it is possible for Li to be present on the electrode in small quantities without being detected as the crystallites may not be aligned properly with the incoming beam to satisfy the Bragg conditions, which can explain the delayed increase in working electrode potential as shown in Figure 2C. Furthermore, some Li might have plated as an amorphous phase, which was undetectable by GI WAXS in operando conditions. The difference in

Li plating behavior confirms that the SEI layer formed when using $LiBF_4$ is better at protecting the plated Li from reacting with protons in the electrolyte, as hypothesized by Li et al.[20]

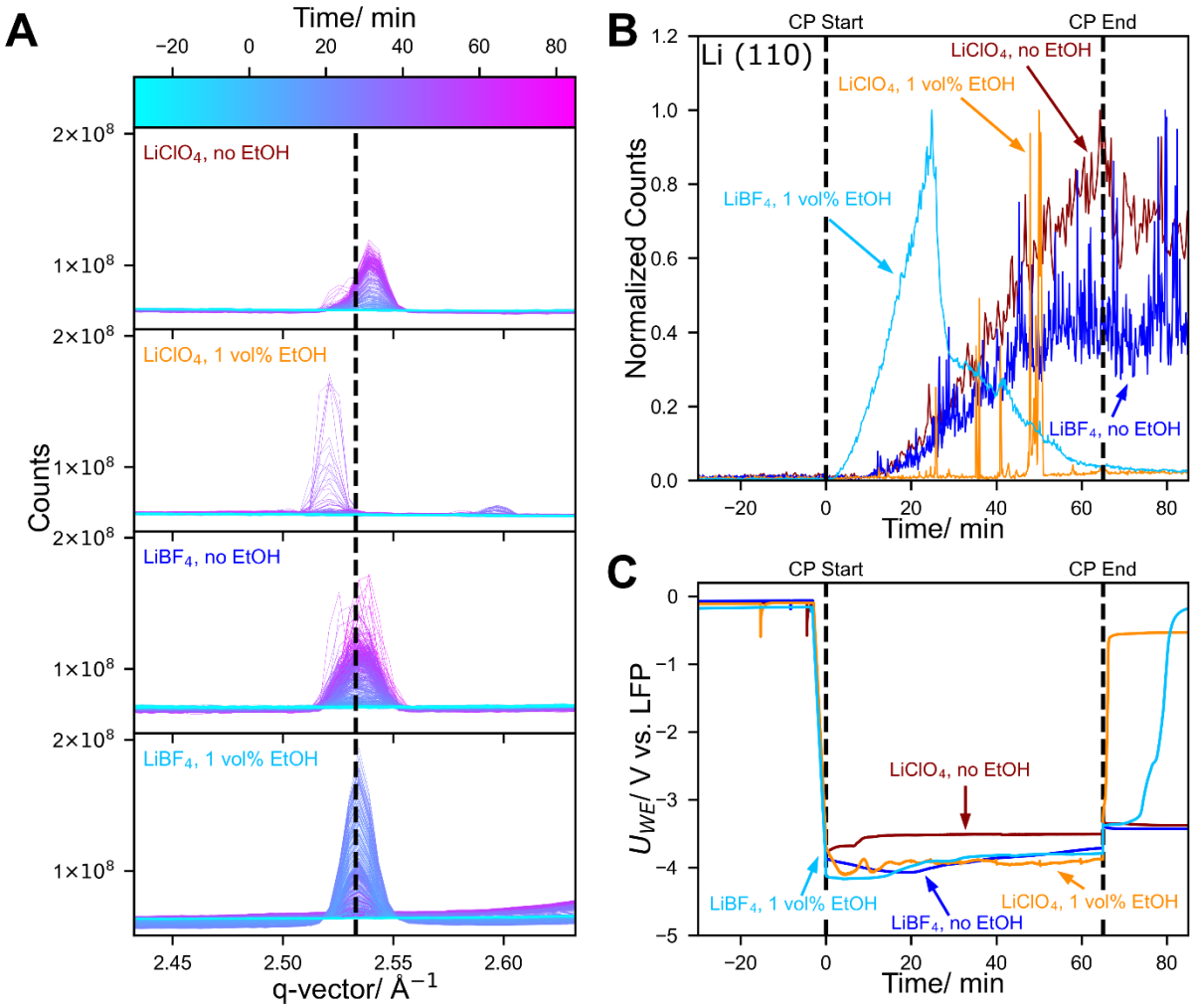

Figure 2: (A) Integrated WAXS patterns showing the Li(110) reflection, measured using different electrolyte compositions. (B) Time development of the Li (110) peak intensities when using different electrolyte compositions. (C) Working electrode potentials in the corresponding experiments. The counter electrode was Pt-mesh and a LFP electrode was used as reference. A 1 M solution of either $LiClO_4$ or $LiBF_4$ in THF with either 0 vol% or 1 vol% EtOH was used as electrolyte. During chronopotentiometry (CP), a current density of -2 mA cm^{-2} was applied.

The observed differences in Li plating behavior point to a substantially different SEI layer formed depending on the electrolyte composition. Previous studies suggest that the SEI layer formed by $LiBF_4$ consists in large parts of LiF.[20] Figure 3A and 3B confirm the formation of crystalline LiF in experiments with $LiBF_4$ containing electrolyte. Notably, peaks corresponding to the LiF were already observed before current was applied to the cell, which indicates that $LiBF_4$ had already partially decomposed to LiF. Figure

3A and 3B show that the intensity of the LiF peak increased slightly during the initial OCV period. This continued decomposition might be facilitated by the X-ray beam.[26] With EtOH, a steep increase in the LiF intensity is observed already at ~-2V vs. LFP during the LSV measurement (Fig. S32, ESI), showing that electrochemical LiF and SEI formation already occurred prior to Li plating. SEI formation before Li plating has previously been confirmed to occur with $LiClO_4$ but not yet with $LiBF_4$.[17,18] However, this steep increase in LiF intensity was not always observed clearly before Li plating potentials were reached (Figure 3A, S52-S54, ESI). As only crystallites above a certain size can be detected with X-ray scattering there is a delay between the formation and the detection of a species, also dependent on cell alignment. Therefore, LiF might have also formed prior to Li plating in other measurements but was not detected until after the LSV measurement. Furthermore, due to the variability of the cell resistance (200-600 Ω) and the resulting difference in ohmic drop (iR) correction, the actual, applied potentials during LSV may vary for different experiments.

Contrary to the non-uniform increase of intensity shown for the Li (110) reflection in Figure 3C, a homogenous increase of intensity over all corresponding detector pixels was observed for LiF, as exemplary shown for the (111) reflection in the $LiBF_4$/ 1 vol% EtOH experiment in Figure 3D, and the ESI (Fig. S55-S57, ESI). This homogeneous increase over all corresponding pixels indicates that polycrystalline LiF composed of small crystallites is deposited. The formation of LiF is most likely accompanied by the formation of BF_3 ($LiBF_4 \rightarrow LiF + BF_3$), which can participate in various organic reactions and therefore might play a critical role in the organic part of the SEI and could possibly explain the better performance of $LiBF_4$ compared to $LiPF_6$.[12,27,28] Even though no quantification based on peak intensities is possible, the high counts observed for all LiF peaks suggest that substantial amounts are formed. It should be noted that at higher q-vectors splitting of LiF peaks appeared, as shown in the ESI (Fig. S10, S13, ESI). This splitting is likely caused by the parallax effect from the formation of multiple separate deposits of LiF on

the working electrode, possibly a consequence of a non-uniform current density distribution due to the electrode configuration.

As more Li is plated, the intensity of LiF peaks decreases (Fig. 3A, 3B, S52, S53, ESI), suggesting that parts of the LiF are lifted above the X-ray beam, as Li plates below it. An inverse trend for the development of the Li and LiF peaks was observed both with and without EtOH in the electrolyte, as depicted in Figure 3E and 3F. Due to its low solubility[29] and high electrochemical stability[30,31] it is unlikely that decreases in LiF intensity were caused by a reaction or dissolution of LiF. These results show that, as previously predicted[13,20], LiF is a key compound in the SEI layer, that can limit proton transport to the plated Li (Fig. 3E, 3F). Experiments with EtOH showed an overall increase in LiF intensity while a current was applied. Continuing LiF formation might prove problematic for long-term stability as it irreversibly removes Li^+ ions from the electrolyte.

As shown in Figure 3B, when EtOH was used in the electrolyte, after 25 min of applied current the intensity of peaks corresponding to Li steeply decrease in intensity for ~ 4 min, coinciding with an increase of intensity for LiF peaks and the appearance of new peaks. Corresponding time traces shown in Figure 3B have been smoothed using Savitzky-Golay filtering. The raw data is available in the ESI (Fig. S54, ESI) This very dynamic behavior in the observed species could indicate the formation of a crack in the protective SEI layer accompanied by reactions of Li with the electrolyte, forming new species as depicted in Figure 3F. Crack formation is a phenomenon well-known in Li metal batteries.[32–35] Furthermore, ex-situ studies of this system have shown a more porous SEI layer when EtOH is present, potentially caused by the formation of hydrogen bubbles when protons are reduced.[14] Crack formation might therefore be initiated by gas formation. As the X-ray beam is only 6 µm wide this is likely a local occurrence and not representative of the whole electrode, suggesting that deposits are not homogeneously distributed over the whole electrode. This phenomenon is an uncontrolled process that could explain varied results between repeat experiments (Fig. S53, ESI). In future studies it might be

advantageous to measure more spots on the electrode. After the steep decrease, the Li peak intensities continue to decrease with a smaller slope suggesting that the protective SEI has partially reformed. Some of the appearing peaks can clearly be attributed to LiH (Figure 3B, S9-S10, ESI). LiH formation has been suggested previously[20,36], but here we provide experimental proof of LiH formation in the Li-NRR. It has been demonstrated previously that LiH can form from the reaction of H_2 with Li in inorganic electrolyte solutions ($\frac{1}{2}H_2 + Li^+ + e^- \rightarrow LiH$).[37] Under proton-limited conditions, an electrochemical pathway ($Li + e^- + H^+ \rightarrow LiH$) might be possible. However, LiH is expected to react with protons or EtOH, forming H_2 ($LiH + EtOH \rightarrow Li^+ + EtO^- + H_2$), which explains the decreasing intensity of LiH peaks throughout the rest of the experiment.[37,38] Therefore, LiH formation might be both a consequence and an intermediate of parasitic hydrogen formation. Nevertheless, considerable LiH formation was observed indicating that despite the temporary exposure of Li to the electrolyte, the proton/ EtOH transport to the electrode is limited, which could indicate a quick restoration of the SEI layer. Formation of LiH was also observed in experiments without EtOH for both $LiClO_4$ and $LiBF_4$ (Figure 3A, S4, S6, S15, S17 S58-S59, ESI) which further supports the hypothesis that it is a reaction occurring under proton-limited conditions. Low intensities suggest that this LiH formation is less pronounced and might arise from the decomposition of THF on the anode or impurities (water, alcohols) in the solvent.[39,40] Notably, no LiH was detected when $LiClO_4$ was used with EtOH (Fig. S19, S23-S24, ESI), further indicating that here the SEI does not limit proton transport to the electrode. It should be noted that the LiH surface has been predicted to be active towards ammonia synthesis at Li plating potentials and therefore might also play a role here.[36] Other appearing peaks have been attributed to LiEtO (q-vector = 0.775 $Å^{-1}$), $LiNH_2$ (q-vector = 2.150 $Å^{-1}$), and Li_3N (q-vector = 1.660 $Å^{-1}$). It should be noted that usually species were identified on the basis of multiple reflections, but due to low peak intensities for the aforementioned species only a single peak each could be used. Even though this has been reported by others, it has to be acknowledged that a certain degree of uncertainty is associated with the peak assignment.[18] An

extensive discussion of peak assignments is provided in the ESI (Fig. S60-S66, ESI). In view of the time courses of their intensities, it is nevertheless reasonable to attribute the peaks to reaction products of Li. Assuming correct peak assignment, they indicate that LiEtO and Li_3N formed immediately after SEI cracking, whereas generation of $LiNH_2$ was slightly delayed. This observation is in accordance with the proposed reaction mechanism for ammonia formation in which Li_3N is progressively protonated and experimental proof of intermediate protonated Li-N species.[10,36] However, the protonation of Li_3N was assumed to be fast, whereas the detection of $LiNH_2$ here suggests that at least the final protonation step is slow and potentially rate-limiting. Otherwise, the formation of sufficiently large crystallites to be detected by GI WAXS is unlikely. These results could suggest that the formation of cracks in the SEI layer is beneficial to Li-NRR performance as intermediate species were only observed afterwards. When the SEI layer is too thick, transport of reactants might be insufficient, but this transport limitation is alleviated when cracks are formed. It is also possible that with an intact SEI layer only crystallites, insufficiently large for detection, are formed. Beneficial or not, crack formation and accompanying reactions show that there is dynamic change of the deposits throughout Li-NRR experiments, suggesting a multitude of simultaneous processes. These processes must be understood to enhance Li-NRR performance. Notably, with the only exception being LiF, all observed species disappear almost completely before the end of the CP, highlighting the need for operando investigations.

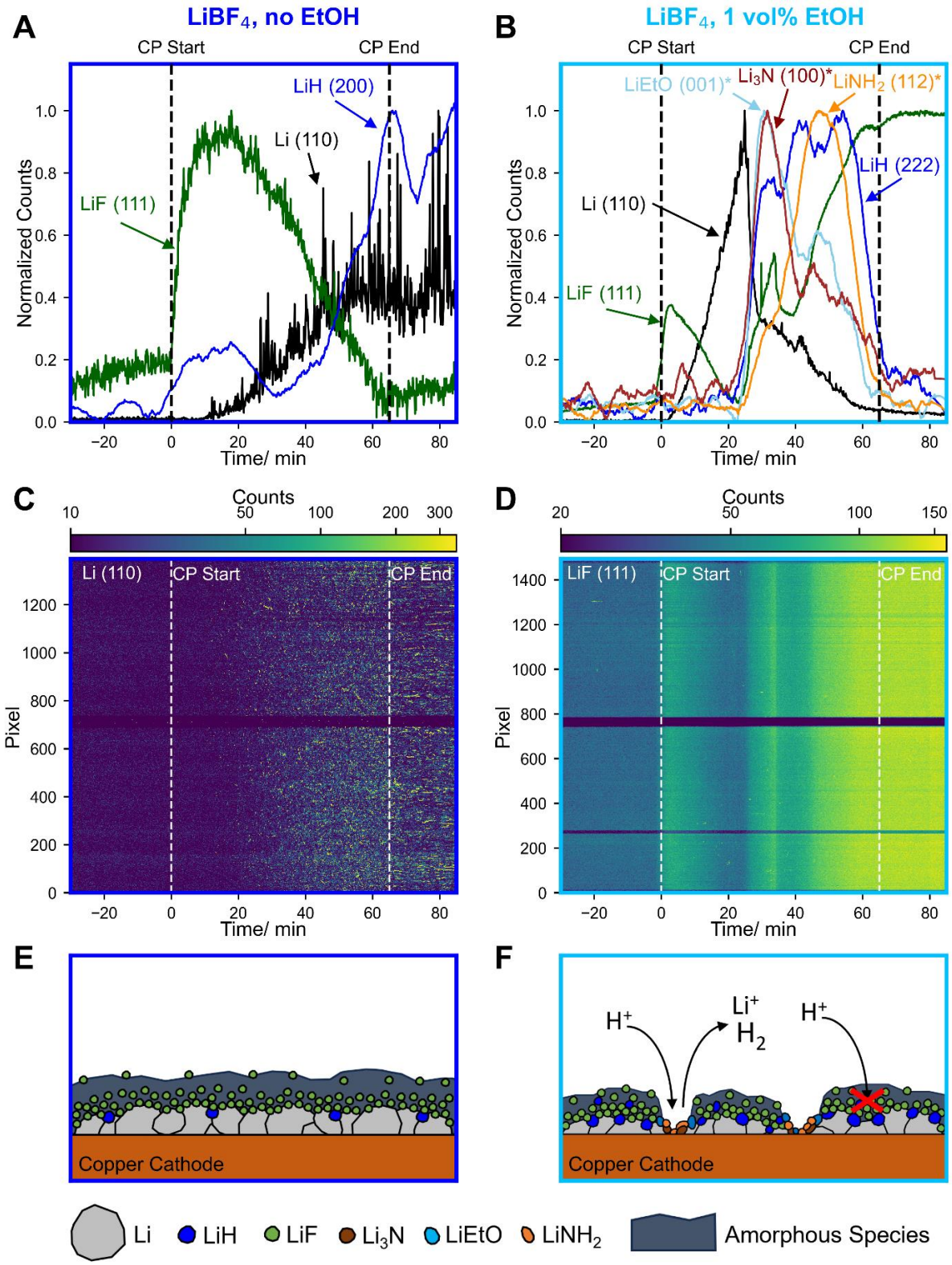

Figure 3: Time development of peak intensities corresponding to observed SEI species and reaction intermediates when using $LiBF_4$ without (A) or with EtOH (B) in the electrolyte. Traces of low intensity peaks (LiH, LiEtO, $LiNH_2$, Li_3N) were smoothed by using Savitzky-Golay filtering. Time development of all detector pixels corresponding to the Li(110) reflection when using $LiBF_4$ without EtOH in the electrolyte (C) and the LiF (111) reflection when using $LiBF_4$ with EtOH in the electrolyte (D). Schematic depiction of crystalline deposits on the working electrode when using $LiBF_4$ without EtOH (E) and with EtOH (F).

When $LiClO_4$ is used as electrolyte salt fewer crystalline species were observed, as shown in Figure 4A and 4B. Remarkably, no LiCl was detected which is in contrast to ex-situ XPS measurements (Fig. S67-S69, ESI) and previous reports.[11,15,20] Ex-situ XPS spectra of the deposits for all electrolyte conditions is provided in the ESI (Fig. S67-S72, ESI). The apparent absence of LiCl in these operando measurements means that the observed ex-situ LiCl is either amorphous or dissolved in the electrolyte and might therefore be detected in residue post experiment. Furthermore, in previous GI WAXS measurements, LiOH and Li_2O were detected.[17,18] Neither Li_2O nor LiOH could be detected clearly in the experiments reported here. A broad increase in intensity around 2.3 $Å^{-1}$ (Fig. S26, ESI), observed when using $LiClO_4$ with EtOH, could correspond to LiOH. For this experiment measurements were conducted on two spots on the electrode, however the signals were only observed on one spot, further showing that deposits are not homogeneously distributed on the electrode during the Li-NRR process. In Figure 4B time traces of Li_2CO_3 peaks, when using $LiClO_4$ with EtOH, are shown. Time traces were smoothed by running averages over 5 values. The raw data is available in the ESI (Fig. S73, ESI).

Li_2CO_3 was generated only with an electrolyte containing EtOH and $LiClO_4$, which might suggest EtOH oxidation. Intermediate species of the multi-step oxidation of EtOH such as acetic acid were detected previously with GC-MS[41], providing a possible pathway to Li_2CO_3 formation. Decomposition products of THF previously detected by NMR[16,19,25], forming only in the presence of EtOH such as 2-ethoxy-THF and γ-butyrolactone provide other possible precursors for carbonate formation. Li_2CO_3 could be observed during the OCV before any current was applied, suggesting that it can also be formed without an electrochemical step, possibly facilitated by the X-ray beam. More Li_2CO_3 signals however, were observed during the CP, indicating that an electrochemical process directly or indirectly facilitates its formation. It should also be noted that not all diffraction peaks are visible at the same time as the peaks arise from single illuminated spots on the detector (Fig. S74-S84, ESI). Therefore, only a small number of Li_2CO_3 crystals were present at any time, explaining why only a partial diffraction pattern can be observed.

These results suggest that Li_2CO_3 is not stable on the electrode and is possibly reduced[42] or dissolved, especially in a proton rich environment[39,43], which could explain the transient behavior shown in Figure 4B. However, the disappearance of a peak does not necessarily correspond to the disappearance of the observed species e.g., a crystal might move and not be aligned to fulfill the Bragg conditions, especially when only a small number of crystals are present. With $LiBF_4$, no Li_2CO_3 was detected, indicating that $LiClO_4$ plays a role as an oxidizer and oxygen source in the formation of Li_2CO_3.

As depicted in Figure 4C, in the absence of EtOH, plated Li is stable on the surface of the electrode. Aside from LiH no crystalline species were detected suggesting that the SEI consists largely of amorphous, likely organic species. In the presence of EtOH, small amounts of Li_2CO_3 are also formed but the SEI layer does not limit proton transport enough for Li to be stable on the surface, as depicted in Figure 4D. Therefore, only a small number of Li crystals is present at a given time, and no stable LiH is formed. The apparent absence of crystalline species, when using $LiClO_4$, as depicted in Figure 4C and 4D is in sharp contrast to the SEI formed from $LiBF_4$. This finding provides a rationale for the reported improvement of FE by adding oxygen or water as this may lead to the formation of possibly crystalline LiOH and Li_2O, which might be beneficial.[11,44]

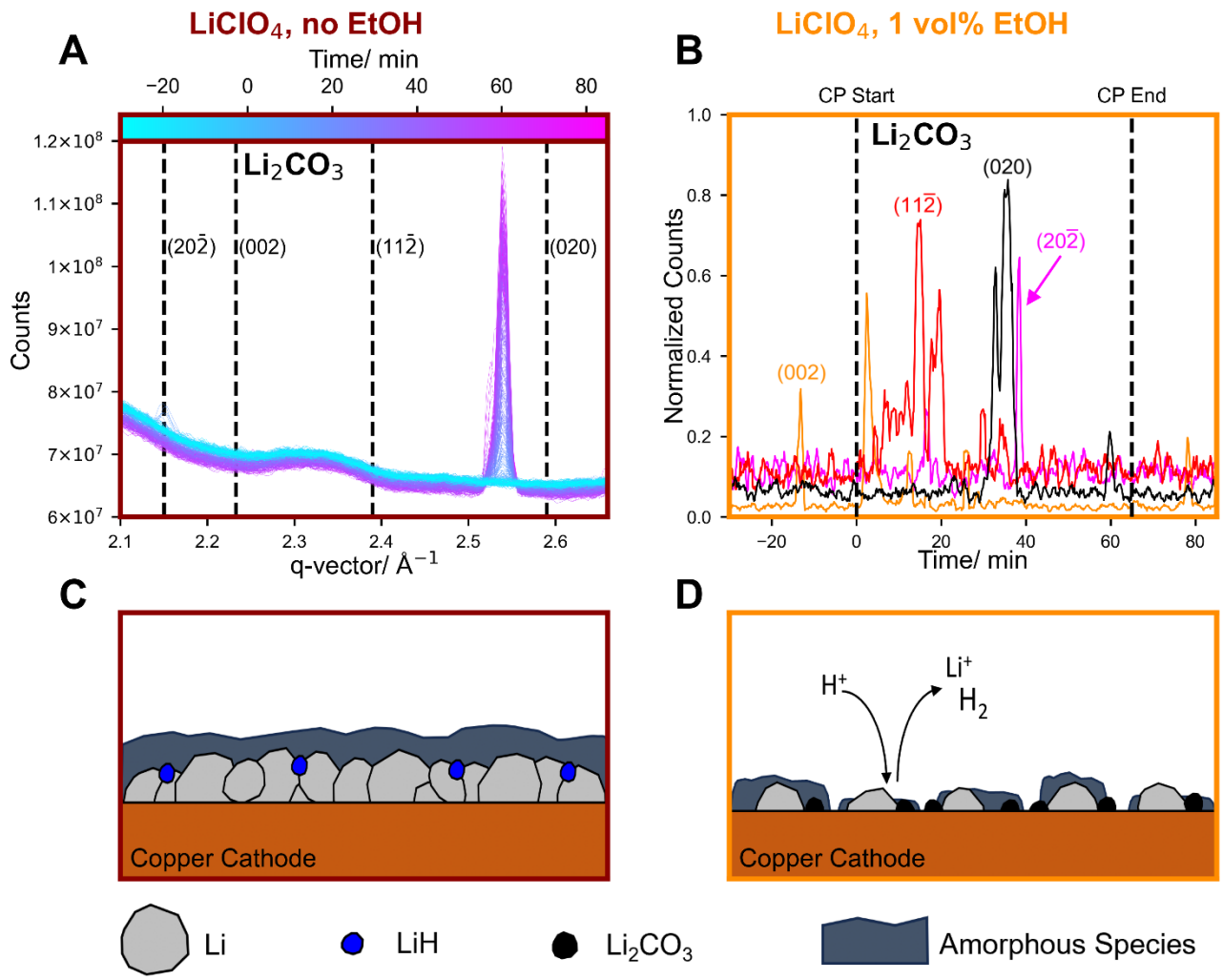

Figure 4: (A) Integrated GI WAXS patterns with Li_2CO_3 reflections marked, using $LiClO_4$ without EtOH in the electrolyte. (B) Time development of Li_2CO_3 reflections, when using $LiClO_4$ and EtOH in the electrolyte. Traces were smoothed by running averages over 5 values. Schematic depiction of crystalline deposits on the working electrode when using $LiClO_4$ without EtOH (C) and with EtOH (D).

In multiple experiments, a restructuring of the Cu (111) single crystal was observed, indicated by a transition from a single crystal refraction pattern to that characteristic of a polycrystalline sample as exemplarily shown in Figure 5A for the $LiBF_4$/ 1 vol% EtOH experiment. This restructuring of the surface and the associated increase in intensity outside of the single crystal refraction spots does not begin before a potential is applied as shown in Figure 5B and the ESI (Fig S58-S59, S85-S94, ESI). Previously, changes to a Mo substrate in the initial minutes of LI-NRR have been attributed to intercalation of Li-ions in a molybdenum oxide layer.[18] In this study, however, no copper oxide is detected, and the substrate

changes occur also at potentials where no oxide would be present. Therefore, this effect might rather be caused by Li plating. However, at room temperature no stable Cu-Li alloy is expected to form.[45] Diffusion of Li ions into Cu electrodes has been reported for anode-free solid state batteries.[46,47] These Li atoms act as nucleation sites for further Li plating[46], which could also lead to roughening and restructuring of the Cu surface. Notably, the surface continues to change even after the experiment when no more current is applied. Clearly there is an interaction of the system with the Cu substrate, justifying future investigation for substrate effects on Li-NRR performance.

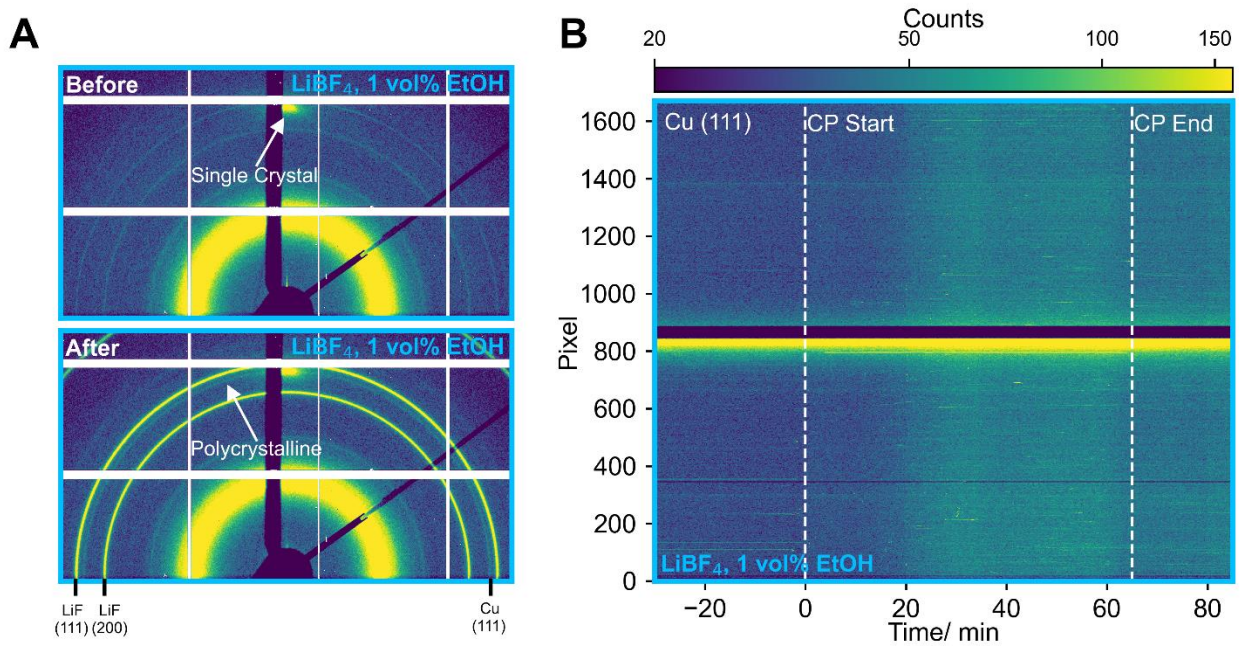

Figure 5: Recorded 2D detector images before and after a Li-NRR experiment (A). Time development of all pixels corresponding to the Cu (111) reflection (q = 3.01 $Å^{-1}$) (B). A solution of 1 M $LiBF_4$ in THF with 1 vol% EtOH was used as electrolyte. During the chronopotentiometry (CP) a current of 2 mA cm^{-2} was applied.

Conclusion

In this work, by using operando GI WAXS, it was shown that unlike the SEI layer formed form $LiClO_4$, the SEI layer formed by $LiBF_4$, limits the proton/ EtOH transport to the electrode, which explains the previously observed higher selectivity towards ammonia. Furthermore, it was confirmed that LiF plays a crucial role in the formation of this beneficial SEI layer. Nevertheless, dynamic changes of the deposits,

such as the formation of cracks in the SEI layer were observed. LiH was identified as another SEI compound which, in contrast to LiF is not stable. Importantly, LiH is likely an intermediate towards the major competing reaction, H_2 evolution, in this system. This report provides experimental proof for LiH formation during Li-NRR, and understanding its formation is critical to mitigating unwanted side reactions, and enhancing NH_3 selectivity. Aside from SEI compounds, intermediate reaction species were observed, demonstrating the presence of intermediate LiN_xH_y species. All observed species showed dynamic behavior over the duration of the experiments, highlighting the multitude of processes occurring during Li-NRR. Finally, Cu substrate-Li interactions were observed, motivating further study into substrate effects on Li-NRR performance. Altogether, these findings inform the molecular design of Li-NRR systems to adequately passivate Li, mitigate HER, promote LiN_xH_y intermediate formation, and consider Li interactions with the cathode. This work motivates achieving a molecular understanding of the SEI resulting from other system enhancements including operating in a flow-cell with hydrogen oxidation on the anode, and inspires new approaches such as the design of artificial SEIs.

Author Contributions

Conceptualization: N.H.D., J.B.V.M., K.L., J.D., I.C.

Data curation: N.H.D., J.B.V.M., K.L., V.A.N., P.B., V.V

Formal Analysis: N.H.D., J.B.V.M., K.L., V.A.N., P.B., S. L., X. F.

Investigation: N.H.D., J.B.V.M., K.L., V.A.N., P.B., V.V

Methodology: N.H.D., J.B.V.M., K.L., V.A.N., P.B., V.V, J.D.

Software: N.H.D.

Supervision: P.C.K.V., T.F.J., J.K., J.D., I.C.

Writing – original draft: N.H.D.

Writing – review & ediding: N.H.D., J.B.V.M., K.L., V.A.N., P.B., V.V., S.L., X.F., P.V., T.F.J., J.K., J.D., I.C.

Conflicts of interest

The authors declare no competing interests.

Acknowledgements

We thank Asger B. Moss for help with writing code. We thank Suzanne Z. Andersen, Jakob B. Pedersen and Mattia Saccoccio for general scientific discussion. We gratefully acknowledge the funding by Villum Fonden, part of the Villum Center for the Science of Sustainable Fuels and Chemicals (V-SUSTAIN grant 9455), Innovationsfonden (E-ammonia grant 9067–00010B) and the European Research Council (ERC) under the European Union's Horizon 2020 research and innovation programme (grant agreement no. 741860). X.F. was supported under the MSCA European Postdoctoral Fellowships (Electro-Ammonia Project 101059643). V.A.N. was supported under the National Science Foundation Graduate Research Fellowship Program under grant no. DGE-1656518 and the Camille and Henry Dreyfus Foundation. We acknowledge the European Synchroton Radiation Facility (ESRF) for the provision of synchrotron radiation using beamline ID 31.

References

1 L. E. Apodaca, *Mineral commodity summaries 2023: NITROGEN (FIXED)—AMMONIA*, National Minerals Information Center, 2023.

2 D. R. MacFarlane, P. V. Cherepanov, J. Choi, B. H. R. Suryanto, R. Y. Hodgetts, J. M. Bakker, F. M. Ferrero Vallana and A. N. Simonov, *Joule*, 2020, **4**, 1186–1205.

3 F. Haber and R. Le Rossignol, *Z. Für Elektrochem. Angew. Phys. Chem.*, 1913, **19**, 53–72.

4 J. Choi, B. H. R. Suryanto, D. Wang, H.-L. Du, R. Y. Hodgetts, F. M. Ferrero Vallana, D. R. MacFarlane and A. N. Simonov, *Nat. Commun.*, 2020, **11**, 5546.

5 Fr. Fichter, P. Girard and H. Erlenmeyer, *Helv. Chim. Acta*, 1930, **13**, 1228–1236.

6 A. Tsuneto, A. Kudo and T. Sakata, *Chem. Lett.*, 1993, **22**, 851–854.

7 A. Tsuneto, A. Kudo and T. Sakata, *Lithium-mediated electrochemical reduction of high pressure N, to NH 3*, 1994, vol. 367.

8 S. Z. Andersen, V. Čolić, S. Yang, J. A. Schwalbe, A. C. Nielander, J. M. McEnaney, K. Enemark-Rasmussen, J. G. Baker, A. R. Singh, B. A. Rohr, M. J. Statt, S. J. Blair, S. Mezzavilla, J. Kibsgaard, P. C. K. Vesborg, M. Cargnello, S. F. Bent, T. F. Jaramillo, I. E. L. Stephens, J. K. Nørskov and I. Chorkendorff, *Nature*, 2019, **570**, 504–508.

9 S. Z. Andersen, M. J. Statt, V. J. Bukas, S. G. Shapel, J. B. Pedersen, K. Krempl, M. Saccoccio, D. Chakraborty, J. Kibsgaard, P. C. K. Vesborg, J. Nørskov and I. Chorkendorff, *Energy Environ. Sci.*, 2020, **13**, 4291–4300.

10 N. Lazouski, Z. J. Schiffer, K. Williams and K. Manthiram, *Joule*, 2019, **3**, 1127–1139.

11 K. Li, S. Z. Andersen, M. J. Statt, M. Saccoccio, V. J. Bukas, K. Krempl, R. Sažinas, J. B. Pedersen, V. Shadravan, Y. Zhou, D. Chakraborty, J. Kibsgaard, P. C. K. Vesborg, J. K. Nørskov and I. Chorkendorff, *Science*, 2021, **374**, 1593–1597.

12 K. Li, S. G. Shapel, D. Hochfilzer, J. B. Pedersen, K. Krempl, S. Z. Andersen, R. Sažinas, M. Saccoccio, S. Li, D. Chakraborty, J. Kibsgaard, P. C. K. Vesborg, J. K. Nørskov and I. Chorkendorff, *ACS Energy Lett.*, 2022, **7**, 36–41.

13 X. Fu, J. B. Pedersen, Y. Zhou, M. Saccoccio, S. Li, R. Sažinas, K. Li, S. Z. Andersen, A. Xu, N. H. Deissler, J. B. V. Mygind, C. Wei, J. Kibsgaard, P. C. K. Vesborg, J. K. Nørskov and I. Chorkendorff, *Science*, 2023, **379**, 707–712.

14 K. Steinberg, X. Yuan, C. K. Klein, N. Lazouski, M. Mecklenburg, K. Manthiram and Y. Li, *Nat. Energy*, 2022, **8**, 138–148.

15 O. Westhead, M. Spry, A. Bagger, Z. Shen, H. Yadegari, S. Favero, R. Tort, M. Titirici, M. P. Ryan, R. Jervis, Y. Katayama, A. Aguadero, A. Regoutz, A. Grimaud and I. E. L. Stephens, *J. Mater. Chem. A*, 2023, **11**, 12746–12758.

16 E. J. McShane, V. A. Niemann, P. Benedek, X. Fu, A. C. Nielander, I. Chorkendorff, T. F. Jaramillo and M. Cargnello, *ACS Energy Lett.*, 2023, 4024–4032.

17 S. J. Blair, M. Doucet, J. F. Browning, K. Stone, H. Wang, C. Halbert, J. Avilés Acosta, J. A. Zamora Zeledón, A. C. Nielander, A. Gallo and T. F. Jaramillo, *ACS Energy Lett.*, 2022, **7**, 1939–1946.

18 S. J. Blair, M. Doucet, V. A. Niemann, K. H. Stone, M. E. Kreider, J. F. Browning, C. E. Halbert, H. Wang, P. Benedek, E. J. McShane, A. C. Nielander, A. Gallo and T. F. Jaramillo, *Energy Environ. Sci.*, 2023, 10.1039.D2EE03694K.

19 H.-L. Du, M. Chatti, R. Y. Hodgetts, P. V. Cherepanov, C. K. Nguyen, K. Matuszek, D. R. MacFarlane and A. N. Simonov, *Nature*, 2022, **609**, 722–727.
20 S. Li, Y. Zhou, K. Li, M. Saccoccio, R. Sažinas, S. Z. Andersen, J. B. Pedersen, X. Fu, V. Shadravan, D. Chakraborty, J. Kibsgaard, P. C. K. Vesborg, J. K. Nørskov and I. Chorkendorff, *Joule*, 2022, **6**, 2083–2101.
21 N. Lazouski, M. Chung, K. Williams, M. L. Gala and K. Manthiram, *Nat. Catal.*, 2020, **3**, 463–469.
22 E. J. McShane, P. Benedek, V. A. Niemann, S. J. Blair, G. A. Kamat, A. C. Nielander, T. F. Jaramillo and M. Cargnello, *ACS Energy Lett.*, 2023, **8**, 230–235.
23 R. Tort, O. Westhead, M. Spry, B. J. V. Davies, M. P. Ryan, M.-M. Titirici and I. E. L. Stephens, *ACS Energy Lett.*, 2023, **8**, 1003–1009.
24 N. Lazouski, K. J. Steinberg, M. L. Gala, D. Krishnamurthy, V. Viswanathan and K. Manthiram, *ACS Catal.*, 2022, 5197–5208.
25 J. B. Valbæk Mygind, J. B. Pedersen, K. Li, N. H. Deissler, M. Saccoccio, X. Fu, S. Li, R. Sažinas, S. Z. Andersen, K. Enemark-Rasmussen, P. C. K. Vesborg, J. Doganli-Kibsgaard and I. Chorkendorff, .
26 H. G. Steinrück, C. Cao, M. R. Lukatskaya, C. J. Takacs, G. Wan, D. G. Mackanic, Y. Tsao, J. Zhao, B. A. Helms, K. Xu, O. Borodin, J. F. Wishart and M. F. Toney, *Angew. Chem. - Int. Ed.*, 2020, **59**, 23180–23187.
27 H. Heaney, in *Encyclopedia of Reagents for Organic Synthesis*, ed. John Wiley & Sons, Ltd, John Wiley & Sons, Ltd, Chichester, UK, 2001, p. rb250.
28 N.-S. Kwon and S.-W. Ryu, *Solid State Ion.*, 2021, **361**, 115563.
29 J. Jones, M. Anouti, M. Caillon-Caravanier, P. Willmann and D. Lemordant, *Fluid Phase Equilibria*, 2009, **285**, 62–68.
30 Y. Zhu, X. He and Y. Mo, *ACS Appl. Mater. Interfaces*, 2015, **7**, 23685–23693.
31 W. D. Richards, L. J. Miara, Y. Wang, J. C. Kim and G. Ceder, *Chem. Mater.*, 2016, **28**, 266–273.
32 R. D. Deshpande and D. M. Bernardi, *J. Electrochem. Soc.*, 2017, **164**, A461–A474.
33 A. Ramasubramanian, V. Yurkiv, T. Foroozan, M. Ragone, R. Shahbazian-Yassar and F. Mashayek, *ACS Appl. Energy Mater.*, 2020, **3**, 10560–10567.
34 W. Lu, L. Sun, Y. Zhao, T. Wu, L. Cong, J. Liu, Y. Liu and H. Xie, *Energy Storage Mater.*, 2021, **34**, 241–249.
35 D. E. Galvez-Aranda and J. M. Seminario, *J. Electrochem. Soc.*, 2018, **165**, A717–A730.
36 J. A. Schwalbe, M. J. Statt, C. Chosy, A. R. Singh, B. A. Rohr, A. C. Nielander, S. Z. Andersen, J. M. McEnaney, J. G. Baker, T. F. Jaramillo, J. K. Norskov and M. Cargnello, *ChemElectroChem*, , DOI:10.1002/celc.201902124.
37 D. Aurbach and I. Weissman, *Electrochem. Commun.*, 1999, **1**, 324–331.
38 T. R. P. Gibb, Jr. and C. E. Messer, 1954.
39 K. Krempl, J. B. Pedersen, J. Kibsgaard, P. C. K. Vesborg and I. Chorkendorff, *Electrochem. Commun.*, 2022, **134**, 107186.
40 G. R. Fulmer, A. J. M. Miller, N. H. Sherden, H. E. Gottlieb, A. Nudelman, B. M. Stoltz, J. E. Bercaw and K. I. Goldberg, *Organometallics*, 2010, **29**, 2176–2179.
41 R. Sažinas, S. Z. Andersen, K. Li, M. Saccoccio, K. Krempl, J. B. Pedersen, J. Kibsgaard, P. C. K. Vesborg, D. Chakraborty and I. Chorkendorff, *RSC Adv.*, 2021, **11**, 31487–31498.

42 B. Han, Z. Zhang, Y. Zou, K. Xu, G. Xu, H. Wang, H. Meng, Y. Deng, J. Li and M. Gu, *Adv. Mater.*, 2021, **33**, 2100404.
43 R. Abegg, F. Auerbach and I. Koppel, *Handbuch der anorganischen Chemie*, Leipzig, S. Hirzel, 1908, vol. 2.
44 M. Spry, O. Westhead, R. Tort, B. Moss, Y. Katayama, M.-M. Titirici, I. E. L. Stephens and A. Bagger, *ACS Energy Lett.*, 2023, **8**, 1230–1235.
45 W. Gąsior, B. Onderka, Z. Moser, A. Dębski and T. Gancarz, *Calphad*, 2009, **33**, 215–220.
46 Y. Huang, H. Chen and L. Nyholm, *Small*, 2023, 2306829.
47 D. Rehnlund, F. Lindgren, S. Böhme, T. Nordh, Y. Zou, J. Pettersson, U. Bexell, M. Boman, K. Edström and L. Nyholm, *Energy Environ. Sci.*, 2017, **10**, 1350–1357.